Characterization of oxide layers formed on 10CrMo9-10 steel operated for a long time in the power industry

Monika GWOŹDZIK[1], Christiane ULLRICH[2], Christian SCHIMPF[2], David RAFAJA[2], Sławomir KULESZA[3], and Mirosław BRAMOWICZ[3]

[1]Czestochowa University of Technology, ul. Dabrowskiego 69, 42-201 Czestochowa, Poland
[2]TU Bergakademie Freiberg, Akademiestraße 6, 09599 Freiberg, Germany
[3]University of Warmia and Mazury in Olsztyn, ul. Michała Oczapowskiego 2, 10-719 Olsztyn, Poland

Abstract. This paper presents the results of diagnostic examinations conducted on the coils of super-heaters made of 10CrMo9–10 steel that were operated in industrial conditions at 480°C for 130 thousand hours. The tube was exposed in a coal-fired boiler. The chemical and phase composition of the oxide/deposit layers formed on both sides of the tube walls (outside – flue-gas side and inside – steam side) and their sequence was examined using optical microscopy, scanning electron microscopy with electron backscatter diffraction and energy-dispersive X-ray spectroscopy, and X-ray diffraction. The changes in the mechanical properties caused by corrosion and aging processes were concluded from the hardness measurements. In addition, the nature of cracks in the oxide layers caused by pressing a Vickers indenter was determined. The results of these examinations have shown a high degradation of steel on the flue-gas inflow side and identified the main corrosion products and mechanisms.

Key words: power industry; 10CrMo9–10 steel; oxide layers.

1. INTRODUCTION

The increasing demand for electricity and heat makes the design of steel for applications in the power industry the subject of interest of numerous scientific centers worldwide [1-7]. Apart from the construction of new power plants, the modernization of existing power units is required in order to increase their operational efficiency. One way, how to increase the operational efficiency of the power units, is to raise the operation temperature of the power equipment. However, a higher operation temperature accelerates the degradation of the used materials via aging and intensified corrosion process [8, 9]. The corrosion process of steel operating for a long time and at elevated temperatures in corrosive atmospheres is substantially affected by the chemical composition of steel, by the operation time of the specific construction element, by the type of the flowing medium, and by the morphology of protective oxide layers [8]. On the steam size, the oxidation of the steel tubes takes place according to the following reactions [10] (1), (2), (3):

$$Fe + H_2O = FeO + H_2, \tag{1}$$

$$2Fe + 3H_2O = Fe_2O_3 + 3H_2, \tag{2}$$

$$3Fe + 4H_2O = Fe_3O_4 + 4H_2. \tag{3}$$
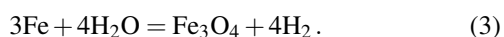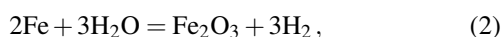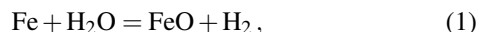
Further reaction products can form if the steam contains impurities stemming, for instance, from the boiler water pollu-

tion. On the side of the exhaust gases, oxidation is driven by the same reactions. However, oxidation can be accompanied by corrosion, which is initiated by the reaction of highly reactive chemical elements from the exhaust gas with the steel or with the iron oxides grown on the surface of the steel pipes. As a result, unwanted deposits can form in addition to the beneficial (protective) oxides. Furthermore, fly ash containing harmful compounds settles on the pipes, where they react with iron oxides and destroy the protective oxide layer [10]. The corrosion of power boilers is the main reason for their failure and one of the main reasons for shutdowns related to their repairs. Because of the diversity of the corrosion mechanisms in power boilers, the sources of corrosion have not been sufficiently explained yet, despite numerous studies. The corrosion inside the boiler depends not only on the fuel type and the combustion conditions, but also on the boiler type and on the location of its individual components [9]. Such components include water wall tubes, which are worn in a completely different way than the steam superheaters. In addition, more intense corrosion occurs on the fire side than on the counter-fire side. Furthermore, the corrosion is intensified during a short-term overheating of the boiler components. Apart from a suitable protective (oxide) layer, also deposits are formed, which do not always play a protective role. Their kind depends typically on the type of fuel used in power plants or thermal power plants (CHPs). Hard or brown coal is still the main fuel, but also biomass (e.g. straw, wood) is more and more often used. In the case of coal-fired facilities, primarily the salts of Na and K, e.g. Na_2SO_4 or K_2SO_4 are produced [11]. Boiler superheater tube failures are the main

M. Gwoździk, C. Ullrich, C. Schimpf, D. Rafaja, S. Kulesza, and M. Bramowicz

problem of forced outages in coal-fired CHP plants. The exhaust gas passes through the superheater pipes, which causes damage during operation. The extent of the damage depends on the quality of the coal, materials used, operation, and maintenance [12]. Similar to the outer wall of the pipe, the inside is also important, which is primarily due to the quality of the water used to generate steam under high pressure. Moreover, it is important to ensure a constant flow of steam at a certain temperature [12]. Otherwise, there is a possibility of a rapid temperature increase, which causes rapid degradation of materials (corrosion) and subsequent failure [8]. Boiler tubes in coal-fired power plants are exposed to harsh conditions, regardless of the side [12]. That is why research related to the oxidation of steel used in the power industry is so important. Low alloy 10CrMo9-10 steel is widely used in the energy industry. There are several papers related to its oxidation at high temperatures [2, 3, 5, 7, 12]. Pramacick et al. [12] examined boiler tubes made of 10CrMo9-10 steel. Researchers found that oxide scales formed inside the pipe during operation. In the case of a considerable thickness of the scale, it was difficult to transfer heat through the pipe wall, which led to local overheating. The formation of oxide scale and its subsequent chipping from the inner wall of the pipe occurred due to improper cleaning and/or poor water quality over an extended period of use. While the tests carried out on the low-alloy 10CrMo9-10 steel [7] concerned the changes on its surface by comparing the thickness of the oxide scale, the chemical composition, and the morphology of the surface of the samples after initial oxidation at 200, 500 and 700°C at different exposure times (5 and 24 h) in wet or dry conditions. It was found that the thickness of the oxide scale increased as a function of temperature and exposure time, with the influence of temperature being more visible than the influence of the exposure time. The presence of water resulted in thicker oxide scales in the tested steel. Lehmusto et al. in [5] found that irrespective of the initial oxidation procedure, an iron oxide scale composed of Fe_2O_3 and Fe_3O_4 was formed on all 10CrMo9-10 steel samples. The thickness of the oxide scale increased as a function of the time and temperature of pre-oxidation. The morphology of the oxide also changed over time. After pre-oxidation, all samples had a chromium-rich area below the iron oxide scale formed, which could slow down further oxidation, resulting in thinner oxides compared to the reference sample.

This contribution is aimed at diagnostic assessment of the progress corrosion in the steam superheater coil, both on the outside and the inside of the tube wall. For this purpose, the recent developments in material analytical techniques, such as scanning electron microscopy (SEM), X-ray diffraction (XRD), atomic force microscopy (AFM) and transmission electron microscopy (TEM) were utilized [13–17]. In particular, SEM and AFM help to study the surface morphology of a large variety of solid materials by sampling their surface heights z(x,y) followed by a numerical derivation of statistical correlations and fractal characteristics [18, 19]. This method demonstrated its applicability in studies of various structures, the surface of polycrystalline diamond compact after soaking in different reagents [18], effect of substrate type on sputtered aluminum

thin films [19]. Aminirastabi et al. [20] used fractal analysis for the modification of a thin layer of $BaTiO_3$.

The research aimed to demonstrate that material science (structural) tests, especially LM, XRD, SEM, as well as numerical methods, mainly fractal analysis, are useful in the characterization of oxide layer structures after long-term operation at elevated temperatures.

2. MATERIAL AND EXPERIMENTAL METHODS

The material under study comprised specimens of the 10CrMo9-10 steel containing 2.23 wt.% Cr, 1.10 wt.% Mo, 0.51 wt.% Mn, 0.18 wt.% Si and 0.12 wt.% C as the main alloying elements taken from steam heater coils operated at the temperature of 480°C for 130,000 hours. The oxide layer was studied on the inner and outer surface of the tube wall and the respective cross-section (Fig. 1). For this purpose, samples with dimensions of 10mm x 10mm were taken from the pipe. The specimens were made transversely to the material axis. The preparation of the metallographic specimen consisted of grinding and polishing. Selected samples were etched in five percent nitric acid.
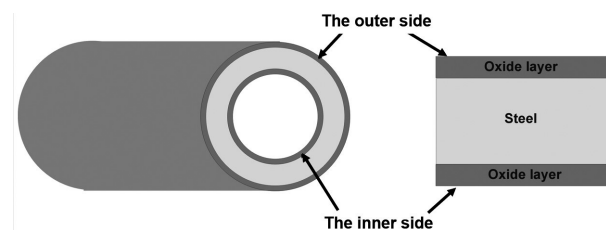

Fig. 1. Positions of the samples used for microstructure analyses

Thorough examinations of the oxide layer that were carried out on the inner and outer surface of the tube wall comprised:
- Microscopic examinations using an optical microscope Olympus GX41 and scanning electron microscopes Jeol JSM-6610LV and Zeiss LEO 1530 Gemini.
- Analysis of the chemical composition using energy-dispersive X-ray spectroscopy (EDS) in conjunction with the scanning electron microscopy (SEM).
- Analyses of the phase composition using X-ray diffraction (XRD) and electron backscatter diffraction (EBSD).
- Thickness measurements of the formed oxide layers.
- Microhardness measurements.

The EDS analyses were performed alternatively on SEM Jeol JSM-6610L, which was equipped with an Oxford EDS electron microprobe X-ray analyzer, and on SEM Zeiss LEO 1530 Gemini with the Roentec EDS detector from Bruker. The XRD experiments were carried out on a Bragg-Brentano diffractometer URD 6 from SEIFERT-FPM. In order to reduce the fluorescence radiation of iron, the $CoK\alpha$ radiation ($\lambda = 1.79026$ Å) was used. The X-ray tube was operated at 40 kV and 30 mA. The XRD patterns were collected in the 2θ range between 15° and 120° with an angular step of 0.01°. The EBSD analyses were done with a Nordlys detector and the software Channel 5 from HKL (Oxford). The microhardness was measured employing the Vickers method using a Shimadzu HMV-G20

2

Bull. Pol. Acad. Sci. Tech. Sci. 69(4) 2021, e137730

microhardness tester. The indentations were performed on the cross-section of the oxide layer at a load of 980.7 mN. Areas without cracks and fissures were selected for testing.

The fractal analysis enabled the characterization of the geometric structures on the surface extending over several orders of magnitude on the length scale. Using fractal geometry, each surface or its profile can be characterized by specifying its fractal dimension (D). A fractal is defined as a self-similar object, i.e. one whose smallest fragment on a given scale is similar to itself. The issues of correlation between fractal parameters and the method of formation and functional features of the surface layer are also interesting. Therefore, an important issue is to learn the relationships related to the fractal description and to improve such methods in correlation with the analysis of the stereometric properties of the surface layer. Standardized methods of numerical analysis also allow us to determine the degree of its directivity, referred to as S_{tr} and corner frequency. Texture anisotropy ratio is a ratio of min/max horizontal lengths of decay of the autocorrelation function whereas corner frequency is a threshold beyond which the allometric dependence ceased for larger-scale lengths.

For the surface mapping in SEM, secondary electrons were used. Surface heights are coded on a grey scale. The first step towards getting spatial characteristics from the SEM images is to compute the autocorrelation function R (4):

$$R(m,n) =$$
$$\frac{1}{(N-n)(N-m)} \sum_{k=1}^{N-n} \sum_{l=1}^{N-m} (z(k+m,y+l) \cdot z(k,l)), \quad (4)$$

where N is the number of measured points, and m, n non-negative integers describing discrete scan shift.

In order to assess the surface morphology, the surface anisotropy ratio S_{tr} can be estimated using the extreme decay lengths of the autocorrelation function along with various directions [21] (5):

$$0 < S_{tr} = \left.\frac{\tau_{a1}}{\tau_{a2}}\right|_{R=1\to 0.2} \leq 1, \quad (5)$$

where a_1, and a_2 are the axes of the extreme autocorrelation decays.

Surfaces are regarded as isotropic when S_{tr} is higher than 0.5, while those with S_{tr} lower than 0.3 are considered anisotropic. Apart from that, the arithmetic mean of the extreme full widths at a half maximum (FWHMs) of the autocorrelation peak along the above directions can be used as a simple yet accurate estimation of the average grain size d_{gr}. Another characteristic can be drawn by making use of the scaling behavior that reveals the self-similarity of the objects upon re-scaling. To this end, the structure function can be used (6):

$$S(\tau_x, \tau_y) =$$
$$\frac{1}{(m-\tau_x)(n-\tau_y)} \sum_{i=1}^{m-\tau_x} \sum_{j=1}^{n-\tau_y} [z(i,j) - z(i+\tau_x,\ j+\tau_y)]^2. \quad (6)$$

Thomas et al. demonstrated that the radially averaged structure function depends allometrically on the scale length τ [22] (7):

$$S(\tau) = K\tau^{2(2-D)}, \quad (7)$$

where D is the fractal dimension and K the pseudo-topothesy. At some point, the structure function quickly changes from exponential into constant one with $2Sq^2$ value with increasing scale length and that threshold is referred to as the corner frequency τ_c.

3. RESULTS

According to the XRD pattern depicted in Fig. 2, the inner side of the pipe contains Fe_2O_3 (hematite), Fe_3O_4 (magnetite), FeO (wustite) and α-Fe (ferrite/α'-martensite). The refined lattice parameters of ferrite and iron oxides are summarized in Table 1. Assuming an increasing oxygen concentration between the core of the tube and its surface, it is expected that Fe_2O_3 is located at the sample surface and followed by Fe_3O_4 and FeO. As the XRD measurements were performed on the sample surface and the penetration depth of X-rays reaches approx. 10 μm in iron oxides, the amounts of the phases located near the sample surface are overestimated in Table 1, while the amounts of the phases located deeper in the samples are underestimated. The optical micrographs of the inner surface confirmed an initial stage of the oxide layer formation (Fig. 3). The macroscopic tests performed showed that the oxide layers formed on the tested steel were discontinuous in places. Superficial damage is clearly visible over a large area of the layer surface in places of small cracks, which then take a more developed form with irregular shapes, reaching deep into the layer.
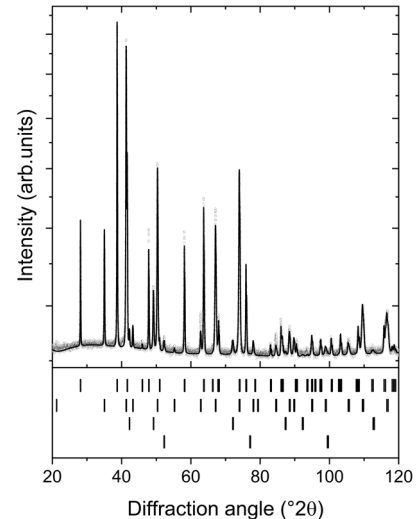

Fig. 2. Diffraction pattern of the inner side of the pipe (small circles) and the Rietveld fit (solid line). The bars in the bottom part of the figure mark the positions of the diffraction lines from Fe_2O_3, Fe_3O_4, FeO and α-Fe (from the top to the bottom)

Quite small but deeper chipping of the layer can be observed. Based on the analysis of the chemical composition (SEM) and X-ray diffraction (XRD), it was shown that three zones have been distinguished in the oxides layer formed. Fe_2O_3 occurs at the surface, followed by magnetite (Fe_3O_4) and wustite (FeO). Microscopic observations show discontinuities in the oxide layers. In the oxide layer produced on the 10CrMo9-10 steel, there are numerous defects in the form of pores and gaps, as shown in

Bull. Pol. Acad. Sci. Tech. Sci. 69(4) 2021, e137730

3

M. Gwoździk, C. Ullrich, C. Schimpf, D. Rafaja, S. Kulesza, and M. Bramowicz

Table 1
Space groups and refined lattice parameters of the phases detected on the inner side of the pipe. The phase amounts are strongly biased by the layered structure of the iron oxides on the surface of the pipe, see text

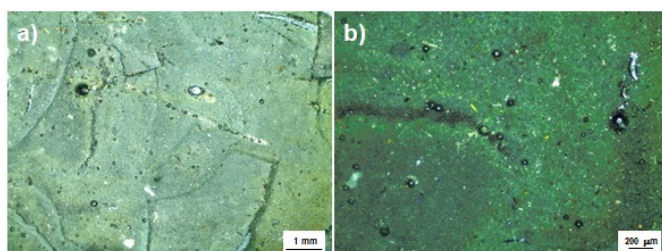| Phase	Space group	Lattice parameters (Å)	Amount (mol.%)
Fe_2O_3 hematite	$R\bar{3}c$	$a = 5.0379 \pm 0.0002$ $c = 13.750 \pm 0.001$	43 ± 4
Fe_3O_4 magnetite	$Fd\bar{3}m$	$a = 8.4126 \pm 0.0003$	53 ± 6
FeO wustite	$Fm\bar{3}m$	$a = 4.3007 \pm 0.0007$	3.4 ± 0.4
α-Fe ferrite/martensite	$Im\bar{3}m$	$a = 2.872 \pm 0.001$	~ 0.6

Fig. 3. Optical micrographs of the oxides formed on 10CrMo9-10 steel of the inner side at elevated temperature

Fig. 4. These defects are the dominant factor causing the chipping and flaking of the oxide layer. The microscopic observations carried out show a large proportion of pores in the layer directly from the steel side. This porosity is oriented parallel to the steel substrate. On the side of the flowing medium, the number of pores present is smaller, but there are areas where the pores become quite large. The voids are probably produced by the diffusion of chromium off the iron oxide layer. From the thermodynamical point of view, Fe_2O_3 and Cr_2O_3 are fully miscible, but the lattice parameters of Fe_2O_3 obtained from XRD correspond to hematite (Fe_2O_3 without chromium). Probably because of the reaction kinetics, Cr oxidizes faster than Fe. Thus, the chromium oxide is leached from the sample surface. Crevice corrosion appears on the oxide layer/steel interface.
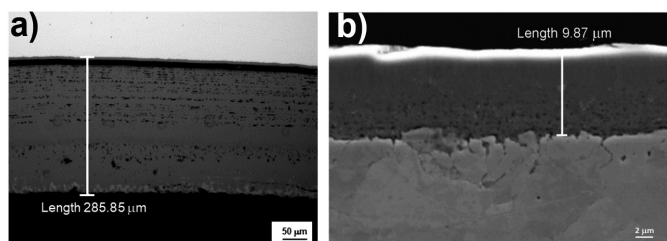

Fig. 4. Cross-section(s) of the inner side of the pipe showing the layered structure of the iron oxides: (a) LM, (b) SEM micrograph taken with secondary electrons

In the interior of the tube directly from the steel side, the magnetite structure is close to the equiaxial, but it becomes columnar with much larger grains from the steam side (Fig. 5). In the interior of the tube directly from the steel side, magnetite with equiaxial grains is enriched with chromium, silicon,
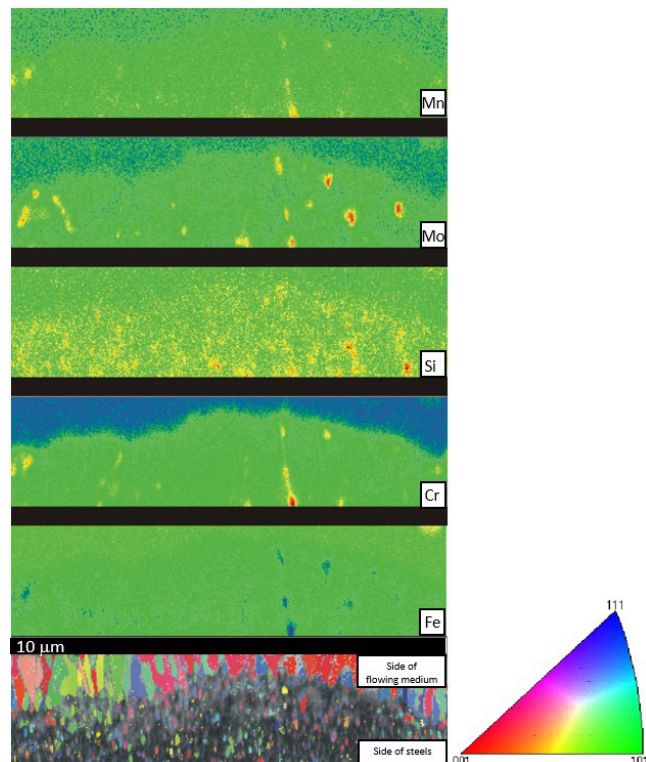

Fig. 5. Upper panel: EBSD analysis of magnetite, the inner side. Different colors indicate different orientations of magnetite grains (s. color map). Other panels: Local concentrations of Fe, Cr, Si, Mo, and Mn

molybdenum, and manganese. In the case of columnar magnetite, other elements precipitate outside of magnetite. On the outer side of the pipe, hematite (Fe_2O_3), magnetite (Fe_3O_4) and bits of ferrite or alpha-martensite were found as well (Fig. 6 and Table 2). However, the dominant crystalline phase was calcium sulphate ($CaSO_4$), as it covers the outer surface of the worn pipe. $CaSO_4$ is a product of the reaction of SO_2 emitted from the burned fuel with $CaCO_3$ (8).

$$CaCO_3(s) + SO_2(g) + 0.5O_2(g) \rightarrow CaSO_4(s) + CO_2(g). \quad (8)$$
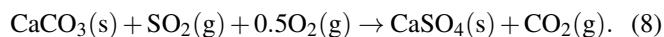
Minor deposits were low quartz (SiO_2) and a phase whose crystal structure is very similar to the chemical composition of sillimullite [23] that has the general chemical formula (Al, Fe, Ti, Mg)$_{8+4x}$Si$_{4-4x}$O$_{20-2x}$ with x = 0.02. The presence of these phases was substantiated by the results of the EDX analysis, which revealed 68 at. % O, 9.6 at. % Si, 7.5 at. % Al, 5.9 at. % S, 5.2 at. % Ca, 1.5 at. % Fe and 0.3 at. % Ti on the outer surface of the worn pipe. As shown by the (macro and microscopic) tests, the oxide/sediment layer on the outer side was characterized by a more attacked surface as compared to the inner side (Fig. 7). The macroscopic tests performed showed that the oxide layers formed on the tested steel were discontinuous in places. Superficial damage is clearly visible over a large area of the layer surface in places of small cracks, which then take a more developed form with irregular shapes, reaching deep into the layer, down to the steel substrate. Macroscopic observations show that the outer layer consists of deposits under which hematite occurs, as evidenced by the red-brown color of the scratch. Under this layer, iron-black magnetite is visible.

4

Bull. Pol. Acad. Sci. Tech. Sci. 69(4) 2021, e137730

The maximum thickness of the oxide layer on the outside the oxide layer with deposits was ∼ 340 μm.
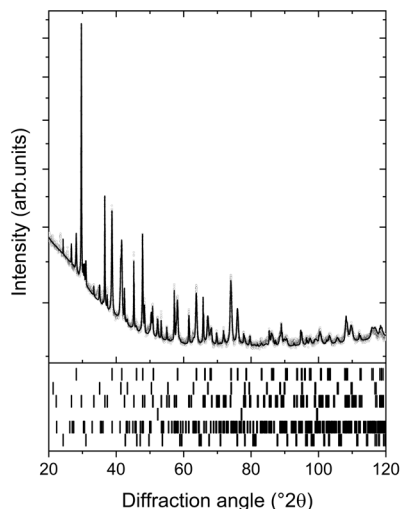

Fig. 6. Diffraction pattern of the outer side of the pipe (small circles) and the Rietveld fit (solid line). The bars in the bottom part of the figure mark the positions of the diffraction lines from Fe_2O_3, Fe_3O_4, $CaSO_4$, α-Fe, "sillimullite" and low quartz (from the top to the bottom)

Table 2
Crystalline phases identified by XRD on the outer surface of the worn pipe

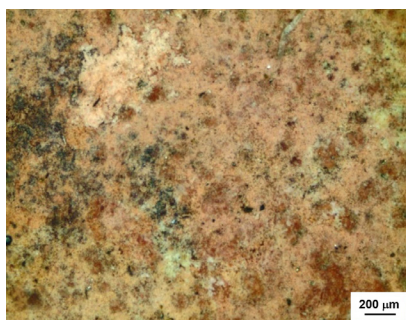| Phase	Space group	Lattice parameters (Å)	Amount (mol.%)
$CaSO_4$	$Amma$	$a = 6.9990 \pm 0.0008$ $b = 6.9897 \pm 0.0008$ $c = 6.2389 \pm 0.0006$	51 ± 2
Fe_2O_3 hematite	$R\bar{3}c$	$a = 5.0371 \pm 0.0006$ $c = 13.744 \pm 0.002$	25 ± 1
Fe_3O_4 magnetite	$Fd\bar{3}m$	$a = 8.406 \pm 0.001$	12 ± 1
α-Fe ferrite/martensite	$Im\bar{3}m$	$a = 2.8720 \pm 0.0009$	1.1 ± 0.1
"Sillimullite"	$Pnam$	$a = 7.567 \pm 0.004$ $b = 7.689 \pm 0.006$ $c = 5.785 \pm 0.003$	8 ± 1
SiO_2 low quartz	$P3_221$	$a = 4.920 \pm 0.002$ $c = 5.419 \pm 0.005$	2.9 ± 0.3

Fig. 7. Oxides formed on 10CrMo9-10 steel of the outer side at elevated temperature

The optical microscopic observations carried out on the cross-section of the oxide layers (Figs. 8a and b) have shown that the oxide layer is seriously degraded on the flue-gas inflow side. Numerous fissures and cracks occur directly on the flue-gas inflow side. The cracks run mainly parallel to the substrate (steel). Additionally, some cracks propagating perpendicularly to the substrate can be observed to a small extent. The oxide layer losses occur mainly in the oxide layer directly on the flue-gas inflow side. On the steel side, cracks have been observed that propagate into the oxide layer. Directly on the steel side, also the oxide layer porosity is smaller, and increases towards the layer interior.
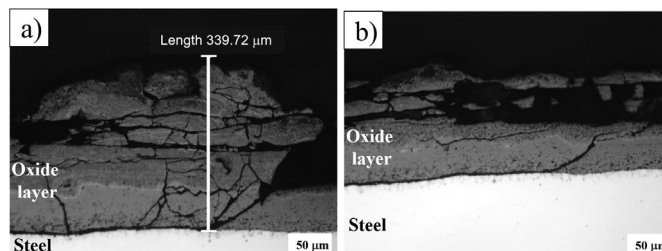

Fig. 8. Optical micrographs of the cross-section of the oxide layers formed on the outer side – different positions (a, b)

In addition, substantial degradation of the bainitic structure can be observed on this side as compared with the inside of the tube wall (Fig. 9). In the case of unstable pipe parameters such as temperature and pressure and considering different thermal expansion coefficients of metal oxides and $CaSO_4$ enriched molten salt, the layer of this salt will easily fall off. After the layer falls off, the flue gas will react with metals, which will result in the pipe resistance to sulfur corrosion [24]. According to the literature [25], the destruction of the oxide layer occurs according to two mechanisms. In the first case, cracking of the layer occurs when the volume of the oxide is much smaller than that of the material on which the oxide has formed, and as a result, the oxide will break, reducing its own deformation. If the volume of the oxide is much larger, it will tend to reduce the deformation energy by breaking adhesion to the substrate material, which will result in flaking and chipping. Corrosion occurs on this side, mainly along the boundaries of the former austenite grain.
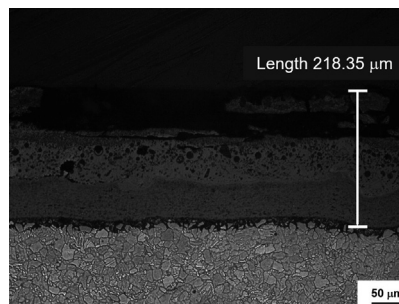

Fig. 9. The delamination between the oxide layer and the steel as seen by optical microscopy on the outer side

The EBSD examinations performed on the magnetite layers that formed on the outer (Fig. 10) side of the tube have shown the magnetite grains are nearly equiaxial. On the outside, di-

Bull. Pol. Acad. Sci. Tech. Sci. 69(4) 2021, e137730

5

rectly on the flue-gas inflow side, areas enriched in silicon oxide (SiO_2) can be observed apart from the iron oxides. Moving towards the original steel substrate, the magnetite layer is enriched with chromium and manganese.
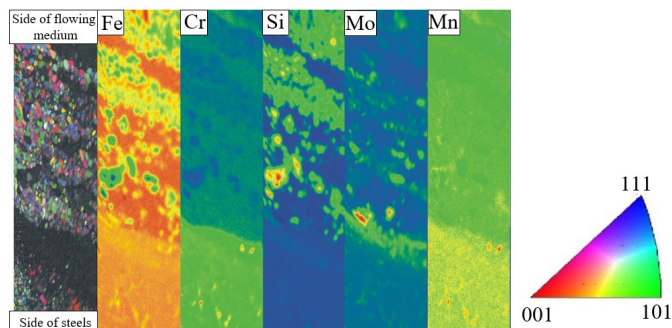

Fig. 10. Left panel: EBSD analysis of magnetite, the outer side. Different colors indicate different orientations of magnetite grains (s. color map). Other panels: Local concentrations of Fe, Cr, Si, Mo, and Mn

Table 3

Spatial characteristics of the inner and outer surfaces of the cylinder: D_1, D_2 – fractal dimensions, τ_1, τ_2 – corner frequencies, S_{tr} – anisotropy ratio, d_{gr} – average grain diameter

Sample	D_1	τ_1 [μm]	D_2	τ_2 [μm]	S_{tr}	d_{gr} [μm]
In	2.32	0.31	2.48	1.48	0.95	1.6
Out	2.48	0.99	2.91	12.4	0.88	2.1

The surface morphology of the iron oxides and deposits was described in terms of the average grain diameter, anisotropy ratio, fractal dimension and corner frequency. These parameters are summarized in Table 3 for the inner and outer surfaces of the pipe. The grain diameter was estimated using the average half-width-at-half-maximum of the autocorrelation peak as shown in Fig. 11. Likewise, the anisotropy ratio was determined using the ratio of lateral decay lengths of the autocorrelation function from unity down to 0.2, respectively, as shown in Fig. 11.
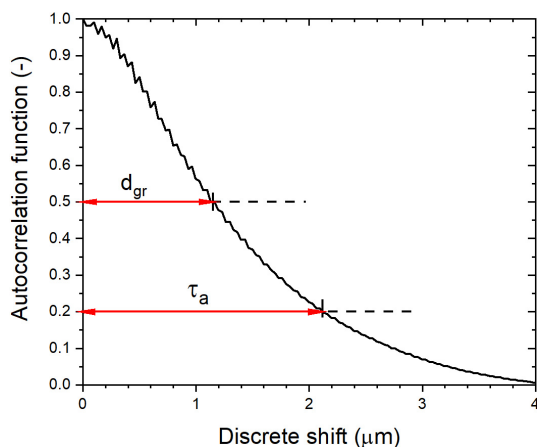

Fig. 11. Example of the autocorrelation function demonstrating the method of estimation of the grain size d_{gr} and lateral autocorrelation length τ_a

On the other hand, fractal dimension and corner frequency were obtained from the double-log plots of the structure func-
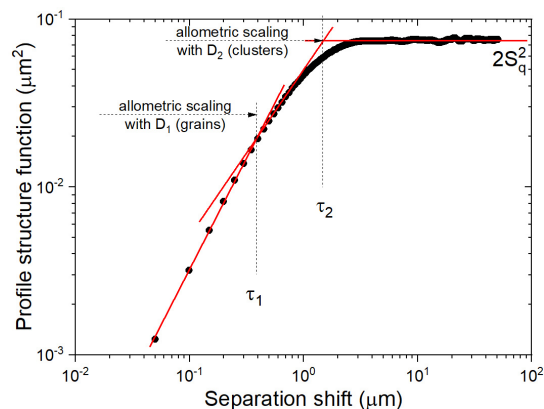

Fig. 12. Example of a log-log plot of the structure function demonstrating the method of estimation of the fractal dimension D and corner frequency τ that separates scaling behaviors of structures of various orders (particles and their aggregates)

tion, as in Fig. 12. The SEM measurements performed on the respective surface (Fig. 13) revealed a mixture of the iron oxides on the steam side and a mixture of the iron oxides and deposits on the gas side. In the case of the outer side, local damage of the deposit layer can be observed. Figure 13 presents SEM images of the inner and outer surfaces of the steel tubes which illustrate the structural changes caused by chemical corrosion. Both images reveal lumpy, well-developed surfaces covered with regular bits of solid material, although with different morphological characteristics. Inner surface (Fig. 13a) is made of a mixture of particles the vast majority of which approaches 10 μm in diameter. Approximately half of these particles are regular, smooth spheres, while the remaining half takes the form of irregular, pitted pieces of the material. On the other hand, the outer surface of the tube is covered with many rounded, tiny grains not exceeding few micrometers in diameter. Because of their small sizes, these particles are not covered with holes, although they tend to aggregate into larger clusters.
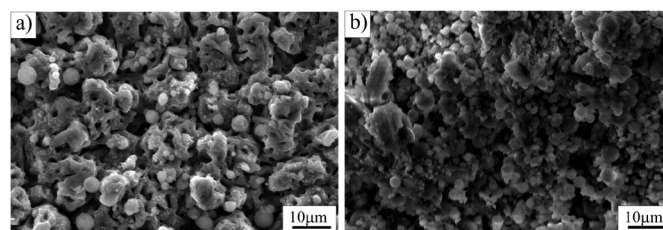

Fig. 13. SEM images (85×58 μm^2) of the corroded surfaces of the pipe: (A) inner surface, (B) outer surface

Table 3 summarizes the spatial characteristics of the surfaces derived from SEM images. Both surfaces turn out to be bifractal, which means that that there are two regimes of the allometric scaling behavior, as seen in Fig. 12. Differences in the scaling exponents can be traced back to the cluster morphology of the structures on the surface reflected by alignment patterns of various length orders. The first regime, limited to the elements of the clusters, is described by the fractal dimension D_1, which determines the relative scaling behavior of the surface variations between the particles, and the corner frequency τ_1, that

6

Bull. Pol. Acad. Sci. Tech. Sci. 69(4) 2021, e137730

sets up the long wavelength cut-off for this behavior. Due to its lower fractal dimension D_1, the inner surface turns out to be less jagged, and thereby less developed, than the outer one (2.32 vs. 2.48). Also, quickly vanishing autocorrelation function is responsible for very low corner frequency τ_1 in the inner surface (310 nm), which is at least an order of magnitude lower than the dimension of predominant morphological features seen in SEM image (Fig. 13a) and one-fifth of the average grain dimension d_{gr}. Such a sharp decay together with a very high anisotropy ratio S_{tr} is likely due to random, although homogeneous distribution of otherwise irregular particles within clusters over the inner surface. On the other hand, the corner frequency τ_1 determined for the outer surface is three times larger than that in the inner surface, and close to the mean size of predominant spherical structures seen in the SEM image (Fig. 13b), although still a half of the mean grain diameter d_{gr}. This coincidence stems from the similarity in the shape and smoothness of the spheres. The remaining fractal parameters, namely fractal dimension D_2 and corner frequency τ_2, are associated with the scaling properties of the entire clusters. As previously, the fractal dimension is found significantly lower in the case of the inner surface (2.48) with respect to the outer one (2.91), but an even larger difference can be found comparing both corner frequencies. Scaling behavior in the outer surface breaks down within a distance almost an order of magnitude longer than that in the inner surface (12.4 vs. 1.48 µm) because of better cluster alignment.

Indentation experiments performed on the outside and the inside have shown that in both cases, there are microcracks, regardless of the hardness values. A greater spread of microcracks was observed in the sediment layer directly from the side of the exhaust gas inflow (Fig. 14). Microscopic observations showed that this layer was brittle and prone to cracks (Figs. 8 and 9). A similar effect was observed on the boundary between the oxide layer and the steel. Less development of microcracks was observed in the dense oxide layer with a small number of pores. In the oxide layer formed on the steam side, the largest microcracks have been observed on the boundary between the oxide layer and the steam.
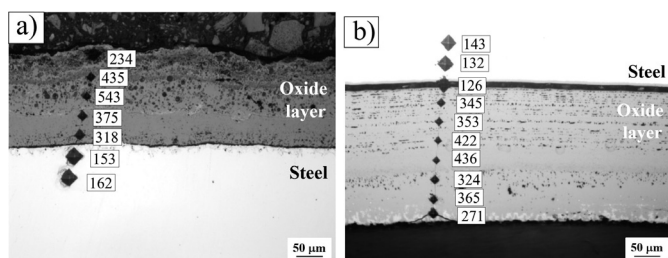

Fig. 14. The indentations produced during the Vickers hardness measurements (HV0.1) on the outer (a) and inner side (b) of the oxide layer

4. DISCUSSION

The obtained results showed that on the side of the vapor flow the oxide layer consists of wustite, hematite and magnetite. Also, in paper [2] Fe_2O_3 and Fe_3O_4 were observed on 10CrMo9-10 steel operated for 200,000 h at the temperature of 525°C. On the other hand, from the side of flue gas in-

flow, apart from the above-mentioned phases, there were also such compounds as $CaSO_4$ or SiO_2. The mechanism of high-temperature corrosion is a very complex phenomenon, depending on both thermal and chemical conditions in the combustion area. As a result of combustion, in the elements of energy devices, thick layers of sediments develop apart from the actual oxide layer, which has an adverse effect. The resulting $CaSO_4$ is the result of flue gas desulphurization, which is used to reduce SO_2 emissions [26]. Recently, many research centers have been analyzing $CaSO_4$. Viklund et al. in paper [27] conducted research on the materials used on superheaters such as 13CrMo44, HCM12A, 304, 317L, Sanicro 28, Hastelloy C-2000, Inconel 625. These materials were operated in power plants that burn waste. The obtained results showed that $CaSO_4$, KCl and NaCl were the main compounds in the formed bed. In addition, molten salt mixtures were also identified. However, the strongest reflections from $CaSO_4$, KCl and NaCl as well as from $CaCl_2$, SiO_2 and Fe_2O_3 were observed on 13CrMo44 steel after 3 h. In paper [24], the authors focused on the study of the corrosion layer formed on the 10Cr18Ni9Cu3NbN steel. The resulting deposits were composed of Al-Si/$CaSO_4$ and Fe_2O_3. Molten salt layer degradation is related to $CaSO_4$ and is formed at the interface between the molten salt layer and metal oxides. The results showed that corrosion progressed faster on the side of the flow of exhaust gases. Therefore, it was recommended to control the sulphur content in the coal, which would reduce the corrosion products formed. The research shows that the main factors that have a significant impact on the formation of deposits are temperature, coal ash composition and particle size. The temperature of the pipe wall and the temperature at the gas outlet from the furnace have a significant influence on the ash deposition. The essential ingredients that remain after combustion are calcium and sulfur. These components affect ash deposition, consequently creating anhydrite [28]. Also, in paper [29], it was shown that calcium sulphate was the main compound formed from convection pass inlet, superheater, and multi-clone inlet. On 10CrMo9-10 steel, the growth of the oxide layer is accompanied by the formation of pores and fissures, which in turn leads to the formation of cracks, which are the initiators of fractures of individual oxide zones occurring in the layer. Initiation of chipping occurs – an oxide layer on the border – steel, between two different oxide layers, inside the same oxide layer. Also, in [30], gaps and chipping were observed at the boundary of two different oxide zones, inside the same oxide zone and at the boundary of the oxide zone – steel. Good cohesion of the oxide layer with the surface of power equipment elements and very slow growth are decisive factors ensuring their quality. Too rapid growth of layers leads to excessive thickness, reduces the clearance of pipelines and superheaters, and due to unfavorable insulation properties, it leads to an increase in the temperature of the elements. Increasingly higher temperature and pressure in the elements of boilers and turbines favor both the excessive growth of layers and the formation of many micropores and cracks in them causing flaking and chipping. Exfoliated oxides can lead to clogging of pipelines and, consequently, local overheating, leading to creeping rupture. Oxide deposits getting into the turbine com-

M. Gwóździk, C. Ullrich, C. Schimpf, D. Rafaja, S. Kulesza, and M. Bramowicz

ponents have a similarly damaging effect. The mechanism of the build-up of oxide layers is based on the core diffusion of iron ions through the oxide because the actual oxidation takes place at the oxide/vapor interface. Magnetite has a little defective crystal structure, hence the diffusion rate of iron ions in its crystal structure is low and the oxide layer grows very slowly. In turn, wustite has a strongly damaged crystal structure, which, regardless of the temperature increase, significantly accelerates the diffusion of iron ions, and thus oxidation. Chrome content 2.0-2.5 wt.% in conventional steels used in the power industry provides a satisfactory resistance to oxidation only up to the temperature of 580°C. Chromium contained in steel is an element with a greater affinity for oxygen than iron, it passes into the oxide in a greater amount than it would result from its relation to iron in steel. Chromium oxidizes with oxygen forming spinel $(Fe, Cr)_3O_4$ with high packing density and low crystal structure defect, effectively slowing down the rate of oxide layer growth. The higher the temperature, the faster the oxidation rate with the same chromium content. Chromium has a decisive influence on the increase of oxidation and corrosion resistance, but the oxidation resistance is also improved by silicon, 1% of which has a similar effect to 4% of chromium. Selective oxidation of chromium is possible as long as a concentration near the steel-oxide boundary is sufficient. The decrease in concentration is compensated by the diffusion of chromium from inside the steel. However, as the temperature increases, the rate of oxidation increases, and the balance between the steel and the oxide is disturbed. This description relates only to the dense, well-adherent oxide layer. Settlement of ash or substances that form easily melting compounds with oxides can cause local destruction of the oxide layer and accelerate oxidation.

The asymmetric shape of the curves of the thickness distribution of the oxide scale suggested local oxidation - corrosion at the grain boundaries. The grain boundaries are responsible for the increased corrosion resistance through the rapid delivery of chromium to the oxide surface [5]. However, after prolonged exposure to an aggressive environment, the grain boundaries are depleted. In the initial phase, the grain boundaries are usually rich in chromium due to the presence of chromium carbides, which favorably influence the steel strengthening mechanisms [17]. Since chromium carbides react with an aggressive environment, this leads to the degradation of the tested steel.

Obtained results are similar to those presented in paper [31]. Researchers showed that the corrosion layer formed on 10CrMo9-10 steel under fuel-oxygen conditions was characterized by large pores in the outer layers and at the boundary between the outer and inner corrosion zones. The main components of the differentiated surface layers were hematite (Fe_2O_3), magnetite (Fe_3O_4) and several Fe-Cr spinels. In addition, the formation of iron sulfide in the surface layer was found. Inline scanning under oxygen-fuel conditions, a distinct chromium-rich internal corrosion zone (on the steel side) was identified.

The study of the surface topography carried out in the paper showed that both surfaces show a bifractal character.

In paper [13], similar results were observed on steel of the same grade, but only from the inside. In paper [13], fractal analysis was performed on three different grades of steel used in the energy industry (13CrMo4-5, 10CrMo9-10, X10CrMoVNb9-1). The tests performed on both the inside and outside walls of the pipe showed the coexistence of two types of structures: large grains with irregular shapes and clusters of smaller grains growing from them. This type of structure was observed in all tested layers except for the oxide layer formed on the 10CrMo9-10 steel, where larger grains were not visible. In this case, the surface was much flatter because there were small grains on it, which resulted in a lower variability of the surface height. Moreover, the obtained results indicated that the tested surfaces showed a high variability of anisotropy - from anisotropic to perfectly isotropic surfaces. In the case of oxides on the inside, a tendency of increasing isotropy with increasing operating temperature was found, while in the case of the outside, such a tendency was not found. Surface topography plays an important role in material science, especially for oxidized surfaces. For this reason, the fractal analysis provides important information about the surface condition of a material applied in the energy industry. The use of fractal analysis in this type of material is important because it provides information about the degree of surface development. The observed cracks in the cross-section of the oxide layer caused by pressing the Vickers indenter were of radial character. According to the literature [32], radial cracks emerge symmetrically from the corners of the cavity. Similar nature of cracks in the cross-section of the oxide layer was observed in [33]. The use of the methodology using crack propagation from the corners of the Vickers imprint resulted in comparable values. There was a greater tendency for radial fractures than for central or Palmqvist fractures. In the case of indenting an indenter into brittle materials, as is the case with sediments, even with light loads, the formation of a recess is accompanied by cracks spreading around the recess. Less development of microcracks was observed in the case of a finer structure and with smaller pore size. Paper [3] describes the texture of the structure on the cross-section of the magnetite layer formed on the 10CrMo9-10 steel during long-term operation at elevated temperatures. The magnetite texture and texture variability were investigated not only on the surface but also as a function of the distance from the surface. Diverse morphology of magnetite at different depths of the layer was found (caused, among others, by the different temperature on the cross-section of the pipe wall during material operation), which is related, among others, to the size of crystallites [2]. Since the presence of texture causes changes in the physical and mechanical properties of the material, it is extremely important to identify the presence of texture in the material.

5. SUMMARY

Based on the microstructure investigations and hardness measurements, the following statements and conclusions can be formulated:

- The deposit/oxide layers formed on the outside of the tube wall experienced higher degradation than the oxide layer formed on the inside.

8

Bull. Pol. Acad. Sci. Tech. Sci. 69(4) 2021, e137730

- Local cases of oxide layer spalling are initiated mainly on the oxide layer – oxide layer boundary, inside the oxide layer itself and occasionally on the oxide layer - steel boundary.
- On the flue gas inflow side, on the oxide layer - steel boundary, there is progressing corrosion along the grain boundaries, additionally, the structure on this side is degraded to a large extent.
- On the flue gas inflow side, iron oxides and deposits based on Ca, S, Na, Al, and Si were found.
- The EBSD mapping performed on well-developed magnetite revealed small equiaxial grains on the flowing medium side, directly on the steel side, which become columnar towards the bulk steel. On the flue gas inflow side, no columnar magnetite has been observed.
- The results of the fractal analysis demonstrated degradation of the oxide structure. As it turns out, the geometric structure of the surface of the oxide layers depending on the operating parameters of power devices may correlate with the microcracks that arise.
- The radial cracks (after pressing the Vickers indenter) in the cross-section of the oxide layer are intensified in the deposit/oxide layer formed directly on the side of the flue gas flow (the outer surface of the tube wall) and the vapor flow (the inner surface of the tube wall).
- The hardness measurements on the oxide layer have shown that the oxide layer grown on the tube wall inside is less susceptible to cracking, to laminations as well as to spalling, mainly on the oxide layer – steel boundary. In the case of the tube wall outside, microcracks were observed on this boundary and at the same time, the oxide layer weakening in this place can result from progressing corrosion on the boundaries of the former austenite grains.

REFERENCES

[1] S. Frangini, A. Masci, and F. Zaza, "Molten salt synthesis of perovskite conversion coatings: A novel approach for corrosion protection of stainless steels in molten carbonate fuel cells," *Corros. Sci.* vol. 53, no. 8, pp. 2539–2548, 2011, doi: 10.1016/j.corsci.2011.04.011.

[2] M. Gwoździk, "Analysis of crystallite size changes in an oxide layer formed on steel used in the power industry", *Acta Phys. Pol. A.* vol. 130, no. 4, pp. 935–938, 2016, doi: 10.12693/APhysPolA.130.935.

[3] M. Gwoździk and Z. Nitkiewicz, "Texturing of magnetite forming during long-term operation of a pipeline of 10CrMo9–10 steel," *Solid State Phenomena*, vol. 203–204, pp. 121–124, 2013, doi: 10.4028/www.scientific.net/SSP.203-204.121.

[4] J. Priss, H. Rojacz, I. Klevtsov, A. Dedov, H. Winkelmann, and E. Badisch, "High temperature corrosion of boiler steels in hydrochloric atmosphere under oil shale ashes," *Corros. Sci.* vol. 82, pp. 36–44, 2014, doi: 10.1016/j.corsci.2013.12.016.

[5] J. Lehmusto, P. Yrjas, and L. Hupa, "Pre-oxidation as a means to increase corrosion resistance of commercial superheater steels," Oxid Met, vol. 91, pp. 311–326, 2019, doi: 10.1007/s11085-019-09898-x.

[6] X. Montero and M.C. Galetz, "Effect of different vanadate salt composition on oil ash corrosion of boilers," Oxid Met, vol. 89, pp. 395–414, 2018, doi: 10.1007/s11085-017-9795-4.

[7] J. Lehmusto, D. Lindberg, P. Yrjas, and L. Hupa, "The effect of temperature on the formation of oxide scales regarding commercial superheater steels. Oxid Met, vol. 89, pp. 251–278, 2018, doi: 10.1007/s11085-017-9785-6.

[8] M. Gwoździk and Z. Nitkiewicz, "Studies on the adhesion of oxide layer formed on X10CrMoVNb9–1 steel," *Arch. Civ. Mech. Eng.*, vol. 14, pp. 335–341, 2014, doi: 10.1016/j.acme.2013.10.005.

[9] P. Gawron and S. Danisz, "Dostosowanie zakresu badań diagnostycznych wybranych elementów kotłów pracujących w warunkach współspalania biomasy," *Energetyka*, vol. 702, pp. 843–853, 2012 [in Polish].

[10] F. Klepacki and D. Wywrot, "Trwałość wężownicprzegrzewaczy wtórnych w warunkach niskoemisyjnego spalania," *12th Informative and Training Symposium: Maintenance of Thermo-Mechanical Power Equipment. Upgrading power equipment to extend its operating period beyond 300 000 hours*. Wisła, Poland 2010, pp. 29–35 [in Polish].

[11] J. Cheng, Y.P. Wu, L.Y. Chen, S. Hong, L. Qiao, and Z. Wei, "Hot corrosion behavior and mechanism of highvelocity arc-sprayed Ni-Cr alloy coatings," *J. Therm. Spray Technol.*, vol. 28, no. 6, pp. 1263–1274, 2019, doi: 10.1007/s11666-019-00890-0.

[12] A.K. Pramanick, G. Das, and S.K. Das, "Ghosh Failure investigation of super heater tubes of coalfired power plant," *Case Stud. Eng. Fail. Anal.*, vol. 9, pp. 17–26, 2017, doi: 10.1016/j.csefa.2017.06.001.

[13] M. Gwoździk, S. Kulesza, M. Bramowicz, "Application of the fractal geometry methods for analysis of oxide layer". *26th International Conference on Metallurgy and Materials (METAL 2017)*, Brno, Czech Republic, 2017, pp. 789- 794.

[14] P. Monivarman, V.A. Nagarajan, and F.M. Raj, "Mechanical and morphological characterization of discarded fishnet/glass fiber reinforced polyester composite," *Bull. Pol. Acad. Sci. Tech. Sci.*, vol. 68, no. 6, pp. 1385–1391, 2020, doi: 10.24425/bpasts.2020.134646.

[15] J. Iwaszko, "Laser surface remelting of powder metallurgy high-speed steel," *Bull. Pol. Acad. Sci. Tech. Sci.*, vol. 68, no. 6, pp. 1425–1432, 2020, doi: 10.24425/bpasts.2020.135385.

[16] C. Bhargava, J. Aggarwal, and P.K. Sharma, "Residual life estimation of fabricated humidity sensors using different artificial intelligence techniques," *Bull. Pol. Acad. Sci. Tech. Sci.*, vol. 67, no. 1, pp. 147–154, 2019, doi: 10.24425/bpas.2019.127344.

[17] M. Gwoździk, M. Motylenko, and D. Rafaja, "Microstructure changes responsible for the degradation of the 10CrMo9–10 and 13CrMo4–5 steels during long-term operation," Mater. Res. Express, vol. 7, no. 1, p. 016515, 2020, doi: 10.1088/2053-1591/ab5fc8.

[18] C. Hao, F.M. Deng, Z.H. Guo, X. Bo, S. Wang, and X. Zhao, "Fractal dimension of decobalt surface on PDC with different acid corrosion reagents at room temperature," *Diam. Relat. Mat.*, vol. 105, p. 107699, 2020, doi: 10.1016/j.diamond.2020.107699.

[19] F.M. Mwema, E.T. Akinlabi, and O.P. Oladijo, "Effect of substrate type on the fractal characteristics of AFM images of sputtered aluminium thin films," *Mater. Sci.-Medzg.*, vol. 26, pp. 49–57, 2020, doi: 10.5755/j01.ms.26.1.22769.

[20] H. Aminirastabi, H. Xue, V.V. Miti´c, G. Lazovi´c, G. Ji, and D. Peng, "Novel fractal analysis of nanograin growth in BaTiO3 thin film," *Mater Chem Phys*, vol. 239, p. 122261, 2020, doi: 10.1016/j.matchemphys.2019.122261.

[21] W.P. Dong, P.J. Sullivan, and K.J. Stout, "Comprehensive study of parameters for characterizing 3-dimensional surface-topography. 4. Parameters for characterizing spatial and hybrid properties," Wear, vol. 178, no. 1–2, pp. 45–60, 1994, doi: 10.1016/0043-1648(94)90128-7.

M. Gwoździk, C. Ullrich, C. Schimpf, D. Rafaja, S. Kulesza, and M. Bramowicz

[22] T.R. Thomas, B.-G. Rosén, and N. Amini, "Fractal characterisation of the anisotropy of rough surfaces," *Wear*, vol. 232, no. 1, pp. 41–50, 1999, doi: 10.1016/S0043-1648(99)00128-3.

[23] R.X. Fischer *et al.*, "A new mineral from the Bellerberg, Eifel, Germany, intermediate between mullite and sillimanite," *Am. Miner.*, vol. 100, pp. 1493–1501, 2015, doi: 10.2138/am-2015-4966.

[24] Z. Liang, M. Yu, and Q. Zhao, "Investigation of fireside corrosion of austenitic heat-resistant steel 10Cr18Ni9Cu3NbN in ultra-supercritical power plants," *Eng. Fail. Anal.*, vol. 100, pp. 180–191, 2019, doi: 10.1016/j.engfailanal.2019.02.048.

[25] M.F. Ashby and D.R.H. Jones, *Engineering Materials 1 An Introduction to Properties, Applications and Design*, Elsevier, 2012.

[26] J. Fernández, F. González, C. Pesquera, A. Neves Junior, M Mendes Viana and J. Dweck, "Qualitative and quantitative characterization of a coal power plant waste by TG/DSC/MS, XRF and XRD," *J. Therm. Anal. Calorim.*, vol. 125, no. 2, pp. 703–710, 2016, doi: 10.1007/s10973-016-5270-8.

[27] P. Viklund, A. Hjörnhede, P. Henderson, A. Stålenheim, and R. Pettersson, "Corrosion of superheater materials in a waste-to-energy plant," *Fuel Process. Technol.*, vol. 105, pp. 106–112, 2013, doi: 10.1016/j.fuproc.2011.06.017.

[28] Y. Wang, J. Jin, D. Liu, H. Yang, and X. Kou, "Understanding ash deposition for Zhundong coal combustion in 330 MW utility boiler: focusing on surface temperature effects," *Fuel*, vol. 216, pp. 697–706, 2018, doi: 10.1016/j.fuel.2017.08.112.

[29] Y. Xie, W. Xie, W-P. Pan, A. Riga, and K. Anderson, "A study of ash deposits on the heat exchange tubes using SDT/MS and XRD techniques," *Thermochim. Acta*, vol. 324, pp. 123–133, 1998, doi: 10.1016/S0040-6031(98)00529-2.

[30] P.J. Ennis and W.J. Quadakkers, "Mechanisms of steam oxidation in high strength martensitic steels," *Int. J. Pressure Vessels Pip.*, vol. 84, pp. 75–81, 2007, doi: 10.1016/j.ijpvp.2006.09.007.

[31] R. Abang, A. Findeisen, and H.J. Krautz, "Corrosion behaviour of selected Power plant materials under oxyfuel combustion conditions," *Górnictwo i Geoinżynieria*, vol. 35, no. 3/1, pp. 23–42, 2011.

[32] T. Aleksandrov Fabijanic', D. Ćorić, M. Šnajdar Musa, and M. Sakoman, "Vickers Indentation Fracture Toughness of Near-Nano and Nanostructured WC-Co Cemented Carbides," *Metals*, vol. 7, 143, 2017, doi: 10.3390/met7040143.

[33] M. Gwoździk and Z. Nitkiewicz, "Scratch resistance characteristic of oxide layer formed on P91 steel," *Inżynieria Materiałowa*, vol. 182, no. 4, pp. 435–438, 2011.

10

Bull. Pol. Acad. Sci. Tech. Sci. 69(4) 2021, e137730